Ag$_3$PO$_4$ Deposited on CuBi$_2$O$_4$ to Construct Z-Scheme Photocatalyst with Excellent Visible-Light Catalytic Performance Toward the Degradation of Diclofenac Sodium

Xiaojuan Chen [1,2], Chunmu Yu [1], Runliang Zhu [2,*], Ning Li [3,*], Jieming Chen [1,4], Shuai Li [1], Wei Xia [1], Song Xu [1], Hailong Wang [1] and Xin Chen [1]

[1] College of Environmental and Chemical Engineering, Foshan University, Foshan 528000, China
[2] CAS Key Laboratory of Mineralogy and Metallogeny, Guangdong Provincial Key Laboratory of Mineral Physics and Material, Guangzhou Institute of Geochemistry, Chinese Academy of Sciences, Guangzhou 510640, China
[3] CAS Key Laboratory of Renewable Energy, Guangzhou Institute of Energy Conversion, Chinese Academy of Sciences, Guangzhou 510650, China
[4] College of Transportation and Civil Architecture, Foshan University, Foshan 528225, China
[*] Correspondence: zhurl@gig.ac.cn (R.Z.); lining@ms.giec.ac.cn (N.L.)

Abstract: CuBi$_2$O$_4$/Ag$_3$PO$_4$ was synthesized through a combination of hydrothermal synthesis and an in situ deposition method with sodium stearate as additives, and their textures were characterized with XRD, XPS, SEM/HRTEM, EDS, UV-Vis, and PL. Then, the photodegradation performance of CuBi$_2$O$_4$/Ag$_3$PO$_4$ toward the degradation of diclofenac sodium (DS) was investigated, and the results indicate that the degradation rate of DS in a CuBi$_2$O$_4$/Ag$_3$PO$_4$ (1:1) system is 0.0143 min^{-1}, which is 3.6 times that in the blank irradiation system. Finally, the photocatalytic mechanism of CuBi$_2$O$_4$/Ag$_3$PO$_4$ was discussed, which follows the Z-Scheme theory, and the performance enhancement of CuBi$_2$O$_4$/Ag$_3$PO$_4$ was attributed to the improved separation efficiency of photogenerated electron–hole pairs.

Keywords: Z-Scheme; CuBi$_2$O$_4$/Ag$_3$PO$_4$; visible light; photocatalytic mechanism

1. Introduction

Diclofenac sodium (DS) is one of the most widely used nonsteroidal anti-inflammatory drugs [1,2]. However, most DS will be excreted outside of the body through urine and stool. Since the removal rate of DS after the treatment of conventional wastewater treatment plants (WWTPs) is no more than 20%, most of the remaining DS would be discharged along with effluents into estuaries, rivers, surface water, ground water, and even drinking water [3–5]. The DS frequently detected in aquatic environments (estuaries, rivers, surface water, ground water, and even drinking water) has aroused great concern in that it endangers human health and poses great risks to the environment [6,7]. Over the last several years, various technologies encompassing adsorption [7,8], photocatalysis [9], Fenton reagents [10], ozonation [11], etc. have been studied to remove DS. Semiconductor photocatalysis is considered a green environmentally friendly and cost-efficient technology [12,13]. However, many of the known photocatalysts such as TiO$_2$ [14,15], CeO$_2$ [16,17], AgCl [18], ZnO [19], etc. have large energy band gaps, making them able to only utilize ultraviolet (UV) light to stimulate their activity. Unfortunately, the region of UV only occupies approximately 4% of the entire solar spectrum, which is just 9.3% of visible light. Considering the above, great efforts have been put in the development of visible-light responsive photocatalysts in recent years [12,13,20].

Silver orthophosphate (Ag_3PO_4), a visible-light responsive photocatalyst with a bandgap of 2.36–2.43 eV, has aroused great attraction since its discovery. [21]. As reported, in the photoelectrocatalysis system of Ag_3PO_4 for water oxidation with a radiation wavelength around 420 nm, a quantum efficiency of approximately 90% could be achieved, which is apparently higher than the referenced semiconductors of approximately 20% (e.g., $BiVO_4$ or N-doped TiO_2) [21]. However, this high efficiency occurs in a system with $AgNO_3$ as an electron scavenger. If the scavenger does not exist, the activity of Ag_3PO_4 would be seriously decreased due to photocorrosion. The photocorrosion of Ag_3PO_4 is closely related to the slight solubility (0.02 g/L) and the reduction of Ag^+ to Ag^0 ($4Ag_3PO_4 + 6H_2O + 12h^+ + 12e^- \rightarrow 12Ag^0 + 4H_3PO_4 + 3O_2$). The above analysis indicated that there still exists a great challenge in maintaining the stability of Ag_3PO_4 in the absence of electron scavengers.

Recently, numerous strategies, including morphology control [22,23], ion doping [24,25], coupling with other semiconductor to construct heterojunction or Z-Scheme composite photocatalysts [26–28], combining with support materials [29–31], etc., have tried to enhance the photocorrosion resistance of Ag_3PO_4. Z-scheme photocatalytic, with a wide absorption range, high charge-separation efficiency, and strong redox ability, not only can overcome the drawbacks of single-component photocatalysts and possesses long-term stability but also can be used to mimic the natural photosynthesis process. Therefore, the construction of Z-Scheme composite photocatalysts has attracted great attention. In order to construct the Z-Scheme composite photocatalysts, appropriate semiconductors of energy band structures matched with Ag_3PO_4 are necessary. $CuBi_2O_4$ is a novel photocatalytic material with a strong visible-light response and excellent photostability [32]. However, previous studies demonstrated that $CuBi_2O_4$ exhibited poor performance on its own, and its composite via doping with other metal oxides semiconductor shows higher activity [33]. Because of the conduction band (CB) potential and valence band (VB) potential of Ag_3PO_4 being more positive than that of $CuBi_2O_4$, theoretically speaking, it is feasible to combine Ag_3PO_4 and $CuBi_2O_4$ to form a Z-Scheme composite photocatalyst.

Thus, in this study, the well-distributed spherical $CuBi_2O_4$ was first prepared under different conditions through the hydrothermal synthesis method and, then, the composite $CuBi_2O_4/Ag_3PO_4$ was further synthesized by the in situ deposition method with sodium stearate as additives. The photocatalytic performances of these catalysts were evaluated for DS photodegradation under visible-light irradiation. Moreover, the photocatalytic mechanism of the catalysts was investigated in detail.

2. Materials and Methods

2.1. Synthesis of CuBi$_2$O$_4$/Ag$_3$PO$_4$

2.1.1. Synthesis of CuBi$_2$O$_4$

$CuBi_2O_4$ with different morphologies were synthesized with the hydrothermal method, which includes four steps. Firstly, $Bi(NO_3)_3 \cdot 5H_2O$ and $Cu(NO_3)_2 \cdot 3H_2O$ were dissolved into moderate volumes of HNO_3 and HNO_3 was prepared to dissolve the $Bi(NO_3)_3 \cdot 5H_2O$ precursor; secondly, the precipitator of NaOH was added into the reaction system. Thirdly, the mixture solution was diluted to a certain volume; fourth, the solution was reacted hydrothermally under 100 °C for 24 h. After the isolation of the produced precipitates by centrifugation, drying of these solids at 60 °C overnight is necessary.

2.1.2. Synthesis of CuBi$_2$O$_4$/Ag$_3$PO$_4$

The in situ deposition method was used to prepare $CuBi_2O_4/Ag_3PO_4$ with sodium stearate as additives. The detailed preparation processes of $CuBi_2O_4/Ag_3PO_4$ for the mass ratio of 1:1 is as follows: 0.1256 g $CuBi_2O_4$ was dispersed into 40 mL of ultrapure water, the solution was ultrasound at 100 W for 15 min subsequently, and then a sodium stearate solution (10 mL, the mole ratio of the sodium stearate to Ag^+ is 2) was added into the reaction system and mechanically agitated for 2 h. After that, an $AgNO_3$ solution (10 mL, 0.9 mmol) was added to the mixture. After stirring for 30 min,

a $Na_2HPO_4 \cdot 12H_2O$ solution (20 mL, 0.3 mmol) was added drop by drop. The precipitate was isolated and washed several times with absolute ethanol and distilled water and then dried at 60 °C overnight.

2.2. Characterization of Photocatalysts

The morphologies of as-prepared catalysts were characterized with JSM-6360LV (JEOL, Tokyo, Japan) and high-resolution transmission electron microscopy (HRTEM, FEI Tecnai G^2 F20 S-TWIN, Hillsboro, OR, USA). The crystal structures of various catalysts were examined with the X-ray diffraction instrument (XRD, Rigaku D/max 2500 PC, Rigaku, Japan). The surface element composition and chemical state analysis were performed on the X-ray photoelectron spectroscopy (XPS) spectra (ESCALAB 250 spectrometer, Waltham, MA, USA). Energy-dispersive X-ray spectroscopy (EDS) was also used to investigate the types and contents of elements in the materials. The nitrogen adsorption–desorption isotherms were obtained using a NOVA-2200e volumetric analyzer (Quantachrome, Boynton Beach, FL, USA). The surface areas of the samples can also be estimated by the BET model. The optical absorption performance of the photocatalysts was analyzed with UV-vis diffusive reflectance spectra labeled by Shimadzu UV-2550 (Kyoto, Japan). The photoluminescence (PL) spectroscopy was detected with a JASCO, FP-6500 florescence spectrophotometer (Oklahoma City, OK, USA).

2.3. Experiments of Photocatalytic Performance

Photocatalytic activity experiments: The photocatalytic activity of as-prepared catalysts was evaluated toward the degradation of diclofenac sodium (DS) as well as dyestuff of Rhodamine B (RhB), Congo red (CR), Methyl Orange (MO), and Methylene Blue (MB). The photoreaction apparatus, equipped with a 300 W Xe lamp and an ultraviolet cutoff filter providing visible light at ≥400 nm, was manufactured by Bilang Biological Science and Technology Co., Ltd., Xi'an, China. The configuration of the apparatus is illustrated in our previous paper [34]. During the experiments, 0.025 g of photocatalyst was added into a 50 mL 10 mg/L DS solution. After the preparation, the adsorption–desorption equilibrium experiment was firstly onset in the dark with magnetically stirred for 30 min. Then, the Xe lamp light was turned on, and the sample was withdrawn at a setting time interval and was filtered with 0.45-μm membrane filters. The pH, concentration of residual DS, and TOC in the filter were detected with the pH analyzer (PHS-3C, Shanghai Jinghong Scientific Instrument Co. Ltd., Shanghai, China), high-performance liquid chromatography (HPLC, Agilent 1260, Santa Clara, CA, USA), and TOC (Shimadzu TOC-$V_{CPH,}$ Kyoto, Japan) analyzer, respectively. As for the photodegradation of dyestuff in the $CuBi_2O_4/Ag_3PO_4$ (1:1) system, the concentration of dyestuff is 15 mg/L and the catalyst dosage is 0.5 g/L.

Photocatalytic stability experiments: The stability of $CuBi_2O_4/Ag_3PO_4$ (1:1) was demonstrated with a repeatability test. The specific experimental processes can refer to the photocatalytic activity experiments. After the reaction in each run, the photocatalysts were collected and vacuum-dried overnight at 60 °C for recycling use.

2.4. Analysis of Reactive Species

The reactive species formed during the photodegradation process of DS were checked with free radical capture experiments, and tert-butanol (t-BuOH), disodium ethylenediamine tetraacetate (EDTA-Na_2), benzoquinone (BZQ) were chose as the scavenger of hydroxyl radical (OH), the hole (h^+), and the superoxide radical (O_2^-), respectively. The detailed free radical capture experiment processes were similar to the photocatalytic activity experiments.

3. Results and Discussion

3.1. Morphology and Associated Formation Mechanism of CuBi₂O₄

Four different experiments under various conditions for the preparation of $CuBi_2O_4$ were firstly conducted to investigate the effect of the morphology and structure on the photocatalytic activity. SEM images of the as-prepared $CuBi_2O_4$ are shown in Figure 1a–d. As shown in Figure 1a, the $CuBi_2O_4$ prepared with 1.2 M NaOH and the step of "dilution" after the addition of NaOH displays well-distributed microsphere structures with diameters of ~4 µm, and its surfaces are comprised of nanometer quadrilateral plates with lengths of ~250 nm and widths of ~200 nm. When the mixture solution of $Bi(NO_3)_3 \cdot 5H_2O$ + $Cu(NO_3)_2 \cdot 3H_2O$ + HNO_3 was diluted before the addition of 1.2 M NaOH, the $CuBi_2O_4$ with a relatively compact and smooth surface are obtained, as described in Figure 1b. Figure 1c,d shows the SEM images of $CuBi_2O_4$ prepared with 2.4 M NaOH, and the step of "dilution" was after or before the addition of NaOH, respectively. The microsphere structural $CuBi_2O_4$ with its surface comprised of tens of nanometers cube was obtained when the 2.4 M NaOH was added before the "dilution", and the $CuBi_2O_4$ with nonuniform size and structure were obtained when the 2.4 M NaOH was added after the "dilution". The remarkable influence of NaOH molarity on the morphology and property of $CuBi_2O_4$ was also evidenced by others. Wang et al. [35] reported the hedgehog-like $CuBi_2O_4$ hierarchical microspheres. Oh et al. [36] reported the three-dimensional spherical $CuBi_2O_4$ nan column arrays connected through non-covalent interactions. Patil et al. [37] reported the spherulitic flower morphology of $CuBi_2O_4$. Xie et al. [38] reported the leaf-like structural $CuBi_2O_4$. Moreover, the order of "dilution" mainly influences the mass transfer rate and Gibbs free energy of the reaction system, finally leading to the formation of different structural crystals to achieve the lowest Gibbs free energy [36].
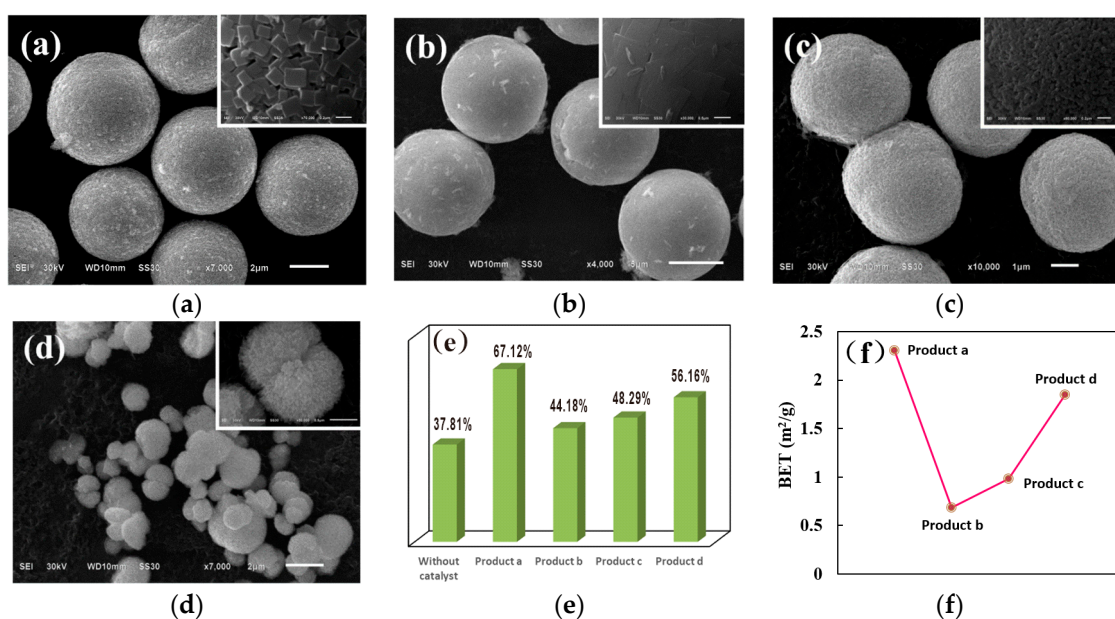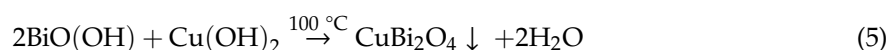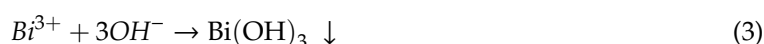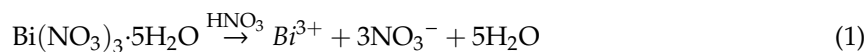

Figure 1. SEM images of $CuBi_2O_4$ obtained in different conditions: (**a**) 1.2 M NaOH and the step of "dilution" was after the addition of NaOH; (**b**) 1.2 M NaOH and the step of "dilution" was before the addition of NaOH; (**c**) 2.4 M NaOH and the step of "dilution" was after the addition of NaOH; and (**d**) 2.4 M NaOH and the step of "dilution" was before the addition of NaOH. (**e**) Photodegradation efficiency of diclofenac sodium (DS) in the catalytic systems of $CuBi_2O_4$ obtained in different conditions. (**f**) Specific surface area of different $CuBi_2O_4$.

On the whole, the mechanism of $CuBi_2O_4$ formation involves three consecutive stages: First, the dissolution of $Bi(NO_3)_3 \cdot 5H_2O$ in HNO_3, as described by the Equation (1); second, the precipitation of $Bi(OH)_3$ and $Cu(OH)_2$ because the solubility product constants of $Bi(OH)_3$ and $Cu(OH)_2$ are 2.9×10^{-7}

and 4.8×10^{-20} (25 °C), respectively, so when the precipitating agent of NaOH was added into the reaction system, the blue flocculent precipitates of $Cu(OH)_2$ formed first, followed by the formation of white precipitates $Bi(OH)_3$, which can be described by Equations (2) and (3); and third, the formation and Ostwald-ripening process of $CuBi_2O_4$, in which the $Bi(OH)_3$ would lose one water molecule first to become partial yellow bismuth hydroxide $BiO(OH)$ under 100 °C (see Equation (4)) and reacted with $Cu(OH)_2$ to form $CuBi_2O_4$ (see Equation (5)) and then the as-formed $CuBi_2O_4$ crystals gave birth to different morphologies via Ostwald ripening.

$$Bi(NO_3)_3 \cdot 5H_2O \xrightarrow{HNO_3} Bi^{3+} + 3NO_3^- + 5H_2O \tag{1}$$

$$Cu^{2+} + 2OH^- \rightarrow Cu(OH)_2 \downarrow \tag{2}$$

$$Bi^{3+} + 3OH^- \rightarrow Bi(OH)_3 \downarrow \tag{3}$$

$$Bi(OH)_3 \xrightarrow{100\,°C} BiO(OH) + H_2O \tag{4}$$

$$2BiO(OH) + Cu(OH)_2 \xrightarrow{100\,°C} CuBi_2O_4 \downarrow + 2H_2O \tag{5}$$

The products of $CuBi_2O_4$ with different morphologies shown in Figure 1a–d were recorded as "Product a", "Product b", "Product c", and "Product d", respectively. Their photocatalytic activity toward DS degradation are described in Figure 1e. As can be seen, all the $CuBi_2O_4$ exhibited more enhanced photocatalytic activity than the self-photodegradation of DS and "Product a" showed the highest catalytic activity, which is consistent with the variation of specific surface area (see Figure 1f). Therefore, "Product a" was used to further synthesize the composite $CuBi_2O_4/Ag_3PO_4$.

3.2. Characterization of $CuBi_2O_4/Ag_3PO_4$

3.2.1. Morphology

The morphology of the as-prepared catalysts are characterized by SEM, and the results are shown in Figure 2. Figure 2a shows the SEM image of Ag_3PO_4, which exhibits an irregular polyhedron structure with an average diameter of approximately 400 nm. Compared with the morphology of $CuBi_2O_4$ shown in Figure 1a, the surface of composite $CuBi_2O_4/Ag_3PO_4$ (1:1) becomes rough (see Figure 2b), which is because the nano-particulate Ag_3PO_4 are attached onto the surface and occupies the nano-sheet gap of the $CuBi_2O_4$'s surface. However, the size of Ag_3PO_4 in the composite is tailored to be approximately ~100 nm, mainly because of the inhibition of the nano-sheet gap of the $CuBi_2O_4$'s surface on the nucleation, growth, and crystallization processes of Ag_3PO_4. Figure 2c shows the lattice fringe image of $CuBi_2O_4/Ag_3PO_4$ (1:1). The observed lattice fringes of 0.267 nm and 0.240 nm correspond to the (210) and (211) planes of Ag_3PO_4, while the *d* spacings of 0.320 nm, 0.426 nm, 0.292 nm, and 0.271 nm can be assigned to the (211), (200), (002), and (310) planes of $CuBi_2O_4$. The composites of prepared $CuBi_2O_4/Ag_3PO_4$ (1:1) were also analyzed by the elemental signature from the EDS spectrum (Figure 2d). The spectrum suggests that the composites are composed of O, Bi, Cu, Ag, and P and that their proportion are 50.34%, 10.30%, 3.10%, 27.47%, and 8.79%, respectively, which further indicates the component of $CuBi_2O_4/Ag_3PO_4$.

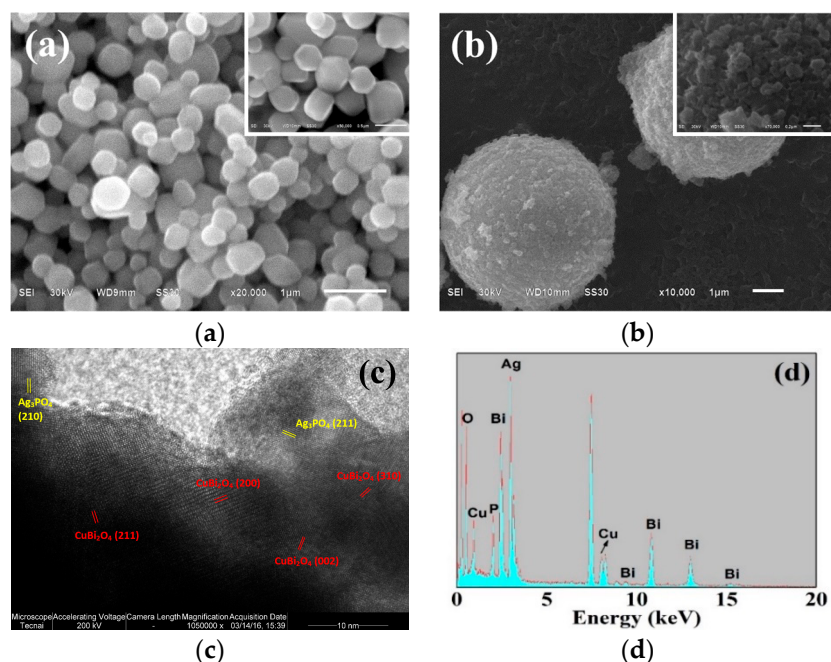**Figure 2.** SEM images of (**a**) Ag$_3$PO$_4$ and (**b**) CuBi$_2$O$_4$/Ag$_3$PO$_4$ (1:1); (**c**) lattice fringe image; and (**d**) Energy-dispersive X-ray spectroscopy (EDS) pattern of CuBi$_2$O$_4$/Ag$_3$PO$_4$ (1:1).

3.2.2. Component and Surface Property

The crystallinity and component of the as-prepared materials were characterized by XRD, and the results are shown in Figure 3. It can be clearly seen that the diffraction peaks in the XRD pattern of Ag$_3$PO$_4$ can be indexed to the phase of Ag$_3$PO$_4$ (JCPDS No. 06-0505) [39]. Moreover, the reflections at 2θ = 20.76, 29.58, 33.20, 36.48, 42.38, 47.75, 52.61, 54.94, 57.19, 61.56, 65.65, 69.80, 71.79, 87.19, and 89.02 are attributed to the crystal planes of (110), (200), (210), (211), (220), (310), (222), (320), (321), (400), (330), (420), (421), (432), and (521), respectively. From the XRD pattern of CuBi$_2$O$_4$, the diffraction pattern shows peaks at 2θ = 20.46, 27.67, 29.21, 30.80, 32.66, 34.25, 37.29, 46.07, 55.05, 59.75, and 65.88, which are in good agreement with the diffractions from (200), (211), (220), (002), (102), (310), (202), (411), (332), (521), and (413), respectively (JCPDS No. 84-1969) [40]. Furthermore, the XRD pattern of CuBi$_2$O$_4$/Ag$_3$PO$_4$ (1:1) suggests that the material obtained just contains CuBi$_2$O$_4$ and Ag$_3$PO$_4$, with the absence of any other substances, indicating that Ag$_3$PO$_4$ couples with CuBi$_2$O$_4$ mainly through the physical effects but not the chemical reaction.
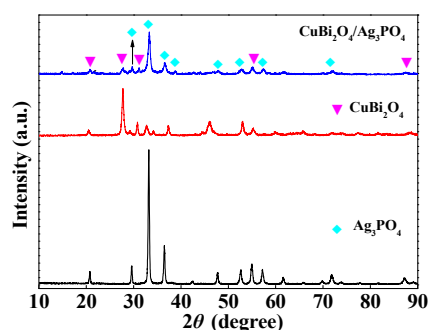

Figure 3. XRD patterns of Ag$_3$PO$_4$, CuBi$_2$O$_4$, and CuBi$_2$O$_4$/Ag$_3$PO$_4$ (1:1).

The chemical compositions and surface chemical states of the CuBi$_2$O$_4$/Ag$_3$PO$_4$ (1:1) composite photocatalyst were further confirmed by the X-ray photoelectron spectroscopy (XPS), as shown in Figure 4. The survey spectrum of CuBi$_2$O$_4$/Ag$_3$PO$_4$ (1:1), shown in Figure 4a, indicates the presence of Cu, Bi, Ag, P, and O. Figure 4b presents the Cu 2p region. It can be clearly observed that the two main

peaks at 934.25 eV and 954.18 eV with a spin-orbit splitting of 20.13 eV are assigned to the binding energies of Cu $2p_{3/2}$ and Cu $2p_{1/2}$, and the two satellite peaks observed at 942.07 eV and 963.25 eV further confirm the Cu^{2+} valence state [41]. Figure 4c shows the core level of the Bi 4f spectra; two bands at 159.13 eV and 164.44 eV corresponding to the binding energies of Bi $4f_{7/2}$ and Bi $4f_{5/2}$, respectively, are observed. The results are consistent with the studies reported by other researchers [36]. Figure 4d shows the Ag 3d region, including two highly intense peaks at 368.16 eV and 374.17 eV, which can be ascribed to the Ag $3d_{5/2}$ and Ag $3d_{3/2}$ binding energies [42,43], respectively. For the high-resolution XPS spectrum of P 2p, shown in Figure 4e, only one peak with the binding energy of 132.90 eV is observed, and it is extremely similar to the 132.40 eV evolved in the PO_4^{3-} [44]. In Figure 4f, the XPS spectrum of O 1s indicating the binding energy of 530.79 eV represents the O-metal bonds, which is in agreement with the reported values of O^{2-} anion coming from $CuBi_2O_4$ and Ag_3PO_4 [41,44].
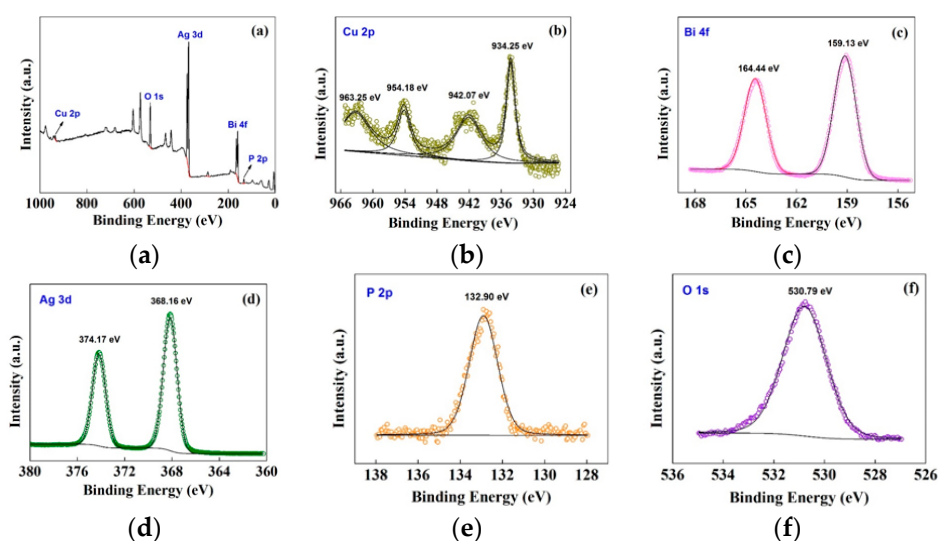

Figure 4. (**a**) XPS survey spectrum of $CuBi_2O_4/Ag_3PO_4$ (1:1) and high-resolution XPS spectra of (**b**) Cu 2p, (**c**) Bi 2p, (**d**) Ag 3d, (**e**) P 2p, and (**f**) O 1s.

3.2.3. Optical Absorption Property

The optical absorption properties of the as-prepared catalysts were determined by the UV-Vis diffusive reflectance analyzer, and the spectra are shown in Figure 5a. Both of the pure $CuBi_2O_4$ and Ag_3PO_4 exhibit strong absorbances in the UV and visible light regions, and their absorbance boundaries are 530 nm and >800 nm, respectively. The results are consistent with the former discovery by other teams [21,45]. In the case of the $CuBi_2O_4/Ag_3PO_4$ (1:1) composite, the absorbance in the visible light regions is much higher than that of the pure Ag_3PO_4. This property can make a positive contribution to the photocatalytic activity of the composite because a more efficient utilization of solar energy could be achieved [46]. In addition, according to the Kubelka–Munk function and the plot of $(\alpha h\nu)^2$ vs $h\nu$ (shown in Figure 5b) [46,47], the band gaps (E_g) of Ag_3PO_4, $CuBi_2O_4$, and $CuBi_2O_4/Ag_3PO_4$ (1:1) were estimated to be 2.42 eV, 1.72 eV, and 2.01 eV, respectively. The band gap energy of $CuBi_2O_4/Ag_3PO_4$ (1:1) is obviously narrower than that of bare Ag_3PO_4, which can conclude that the formed composite is more easily excited by visible light and that the utilization ratio of visible light is enhanced. Furthermore, the band-edge potentials of the conduction band (E_{CB}) and valence band (E_{VB}) could be calculated from the equations [47]: $E_{VB} = X - E^C + 0.5E_g$ and $E_{CB} = X - E^C - 0.5E_g$, where X is the geometric mean of the electronegativity of the constituent atoms (5.96 eV for Ag_3PO_4 and 4.59 eV for $CuBi_2O_4$) [26,48] and E^C is the energy of the free electrons on the hydrogen scale (about 4.5 eV). Thus, the E_{VB} and E_{CB} of Ag_3PO_4 can be estimated to be 2.67 eV/NHE and 0.25 eV/NHE, while the E_{VB} and E_{CB} of $CuBi_2O_4$ can be estimated to be 0.95 and −0.77 eV/NHE, respectively.
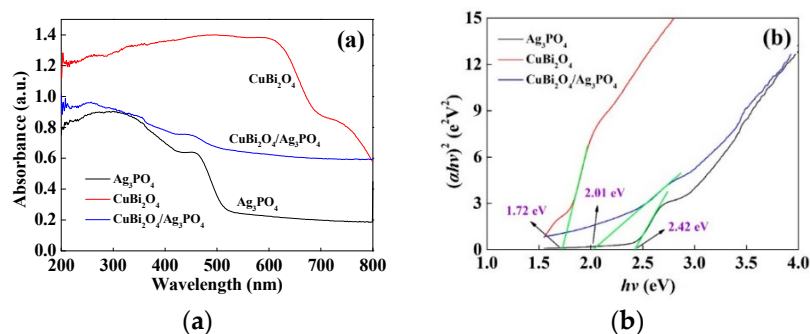
Figure 5. (**a**) UV-vis diffuse reflectance spectra and (**b**) plots of $(\alpha h\nu)^2$ versus energy ($h\nu$) of Ag_3PO_4, $CuBi_2O_4$, and $CuBi_2O_4/Ag_3PO_4$ (1:1).

3.3. Photodegradation Performance of DS in Different Catalysts Systems

In order to estimate the photocatalytic activity of the as-prepared materials, DS was selected as a target pollutant. Figure 6a indicates the photodegradation efficiency of DS in different photocatalytic systems. In the blank irradiation system, the self-photodegradation efficiency of DS during the 120 min of reaction is 37.81%. Under the same conditions, the degradation efficiencies of DS in the pure $CuBi_2O_4$ and Ag_3PO_4 photocatalytic system are 67.12% and 77.84%, respectively. While in the photocatalytic system of $CuBi_2O_4/Ag_3PO_4$ (1:1), the degradation efficiency of DS reaches 85.45%. This suggests that the addition of catalysts promotes the degradation of DS and that there is a synergistic effect between $CuBi_2O_4$ and Ag_3PO_4. A pseudo-first-order kinetic model was employed to fit the experimental data of DS degradation in different photocatalytic systems, and the results are shown in Table 1. It can be seen that the degradation rate constants of DS are 0.0041 min^{-1}, 0.0084 min^{-1}, 0.0112 min^{-1}, and 0.0069 min^{-1} in the photocatalytic system of blank irradiation, $CuBi_2O_4$, Ag_3PO_4, and commercial TiO_2, respectively. The low photocatalytic activity of commercial TiO_2 is mainly due to its weak absorption of visible light, resulting in a small number of active carriers. As for the photocatalytic systems of composite $CuBi_2O_4/Ag_3PO_4$, the rate constant of DS increases firstly and then decreases with the further increase of Ag_3PO_4 content in the composites, which is consistent with the variation of specific surface area (see Table 1). The main reason is that the deposition of excessive Ag_3PO_4 on the surface of $CuBi_2O_4$ will block the gap between the nanosheets on the surface of $CuBi_2O_4$, which is not conducive to the diffusion of reactants and products. Also, when the mass ratio of $CuBi_2O_4$ and Ag_3PO_4 in the composite is 1:1, the rate constant of 0.0143 min^{-1} can be obtained, which is approximately 3.6 times that of the values in the blank irradiation system.

Table 1. Photodegradation rate parameter of DS under different systems.

Catalyst	Specific Surface Area (m^2/g)	K_{app} (min^{-1})	R^2
Blank irradiation	/	0.0041	0.87
$CuBi_2O_4$	2.307	0.0084	0.95
Ag_3PO_4	3.874	0.0112	0.89
Commercial TiO_2	/	0.0069	0.94
$CuBi_2O_4/Ag_3PO_4$ (2:1)	4.938	0.0098	0.92
$CuBi_2O_4/Ag_3PO_4$ (1:1)	7.846	0.0143	0.91
$CuBi_2O_4/Ag_3PO_4$ (1:2)	7.442	0.0138	0.91

To understand the mineralization rate of DS in different photocatalytic systems, the TOC concentrations of the reacted DS solutions were detected and the removal efficiency are described in Figure 6b. In the blank irradiation system, the mineralization rate of DS is 14.36%. When the catalysts of $CuBi_2O_4$, Ag_3PO_4, and $CuBi_2O_4/Ag_3PO_4$ (1:1) were introduced into the reaction system, the mineralization rates of DS increased to be 35.43%, 49.62%, and 57.33%, respectively. Figure 6c shows the change of the solution pH as reaction time goes on at different photocatalytic systems.

In general, the pH of the solution decreases, but there is a fluctuation at a certain time interval in each photocatalytic system, which can be explained by forming some acidic intermediates, and they are decomposed as the reaction time is prolonged.

Figure 6d shows the removal efficiency of various dyes in the catalytic system of $CuBi_2O_4/Ag_3PO_4$ (1:1). It can be seen that, within 20 min, 15 mg/L of RhB and MB can be completely decomposed by 0.5 g/L of the composite photocatalyst, while the removal efficiency of CR and MO are 85.38% and 94.24%, respectively. The results show that the as-prepared $CuBi_2O_4/Ag_3PO_4$ exhibits excellent photocatalytic activity for the degradation of dyes as well.
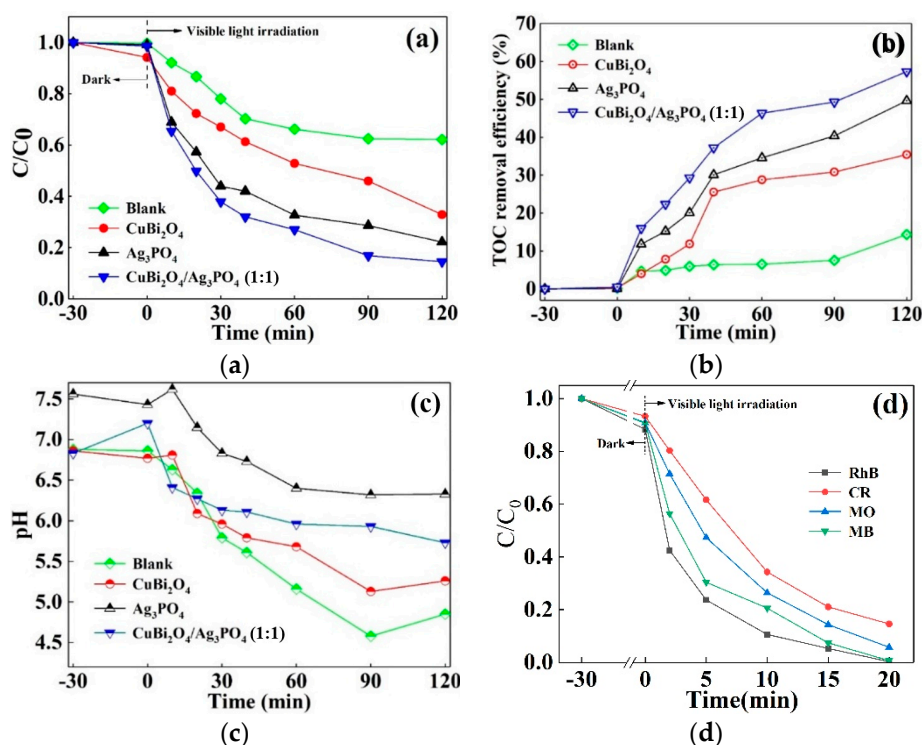

Figure 6. (**a**) Photocatalytic activity of the as-prepared catalysts toward DS degradation under visible light irradiation; (**b**) the TOC removal efficiency and (**c**) changes of pH values in the photodegradation solutions of different catalytic systems; and (**d**) the photocatalytic activity of $CuBi_2O_4/Ag_3PO_4$ (1:1) towards various dyestuff degradation under visible light irradiation.

The stability of the photocatalyst is a very important parameter with regard to practical applications. To further investigate the performance stability of the prepared $CuBi_2O_4$, Ag_3PO_4, and $CuBi_2O_4/Ag_3PO_4$ (1:1), the cycling degradation experiments of DS were carried out and the results are shown in Figure 7a. It is found that the degradation efficiency of DS in the pure $CuBi_2O_4$ photocatalytic system reduced from 67.12% to 63.05% after a 5-time repeated reaction, while the degradation efficiency of DS in the pure Ag_3PO_4 and $CuBi_2O_4/Ag_3PO_4$ (1:1) photocatalytic system reduced by a large extent, i.e., 18.51% and 11.99%. Furthermore, the corresponding XRD results shown in Figure 7b suggest that there is a negligible change about the phase structure of $CuBi_2O_4$ sample after the repeated photocatalytic reactions, further indicating the photocatalytic stability of the $CuBi_2O_4$. However, compared with the XRD spectra of the fresh Ag_3PO_4 and $CuBi_2O_4/Ag_3PO_4$ (1:1), the diffraction peaks readily indexed as the metallic silver (Ag^0) emerge in the XRD spectra of the reacted Ag_3PO_4 and $CuBi_2O_4/Ag_3PO_4$ (1:1). In addition, the appearance of Ag^0 in the reacted Ag_3PO_4 and $CuBi_2O_4/Ag_3PO_4$ (1:1) can be further confirmed by the XPS. Figure 7c shows the high-resolution Ag 3d XPS spectrum of $CuBi_2O_4/Ag_3PO_4$ (1:1) used five times. Based on the Ag 3d XPS spectrum of the fresh $CuBi_2O_4/Ag_3PO_4$ (1:1) (see Figure 4d), the two individual peaks are further divided into four different peaks and the two main peaks at binding energies of 368.16 eV and 374.17 eV can be attributed to the Ag^+ of Ag_3PO_4, whereas

the peaks at 368.32 eV and 374.40 eV can be attributed to the metallic silver (Ag^0). From the result, it is clear that the Ag^0 should have been formed on the surface of the reacted $CuBi_2O_4/Ag_3PO_4$ (1:1) and that the proportion of the peaks relative to Ag^0 occupy 5.52% of the total fitting peak area. However, the Ag 3d XPS spectrum of the reacted Ag_3PO_4 shown in Figure 7d indicates that the formed Ag^0 in the surface of Ag_3PO_4 is 11.78%, which is much higher than that in the reacted $CuBi_2O_4/Ag_3PO_4$ (1:1), further implying the enhanced stability of the $CuBi_2O_4/Ag_3PO_4$ (1:1) in comparison to pure Ag_3PO_4.
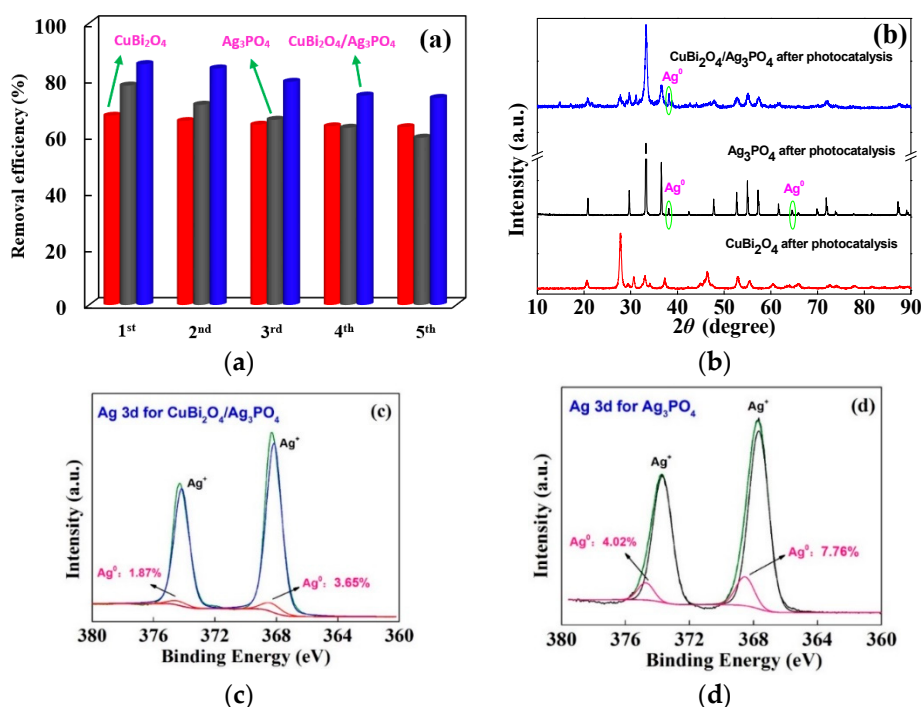

Figure 7. (**a**) Photodegradation efficiency of DS in different recycle runs with the various photocatalysts of $CuBi_2O_4$, Ag_3PO_4, and $CuBi_2O_4/Ag_3PO_4$ (1:1); (**b**) XRD pattern of the photocatalysts used for five recycling; (**c**) XPS spectrum of Ag 3d for the catalyst $CuBi_2O_4/Ag_3PO_4$ (1:1) recycled five times; and (**d**) XPS spectrum of Ag 3d for the catalyst Ag_3PO_4 recycled five times.

3.4. Photocatalytic Mechanism of Different Catalysts

Photoluminescence (PL) is a useful tool for obtaining information about the photogenerated electron–hole recombination property of materials, which helps us to understand the photocatalytic mechanism of the catalysts. Therefore, the PL spectra of the as-prepared $CuBi_2O_4$, Ag_3PO_4, and $CuBi_2O_4/Ag_3PO_4$ (1:1) were first recorded at room temperature with a excitation wavelength of 500 nm, and the spectra are shown in Figure 8a. Obviously, the PL intensity of the $CuBi_2O_4/Ag_3PO_4$ (1:1) composite is much lower than that of the pure $CuBi_2O_4$ and Ag_3PO_4, indicating that the combination of $CuBi_2O_4$ and Ag_3PO_4 has effectively improved the photogenerated carriers' separation. Therefore, though a small amount of Ag^0 has formed on the surface of $CuBi_2O_4/Ag_3PO_4$ (1:1), its photocatalytic performance is still enhanced compared with the pure $CuBi_2O_4$ and Ag_3PO_4.

Moreover, the free radical capture experiments were designed to investigate the difference of main reactive species in the photocatalysis systems of blank irradiation, $CuBi_2O_4$, Ag_3PO_4, and $CuBi_2O_4/Ag_3PO_4$ (1:1). Generally speaking, when the scavenger is added into the reaction system, if the degradation efficiency of the target contaminant do not change significantly, it indicates the weak effect of the captured reactive species on the photodegradation of the target pollutant, while if the degradation efficiency of the target contaminant is inhibited in a great degree, it indicates the captured reactive specie is involved in the photodegradation of the target pollutant and that the contribution of the reactive species is greater with the increased inhibition efficiency. Figure 8b–e shows the photodegradation efficiency of DS under various scavengers in different photocatalytic systems. From

Figure 8b, O_2^- is the major reactive species in the self-photodegradation process of DS, while the effect of h^+ and OH can be ignored. In the photocatalytic system of the pure $CuBi_2O_4$, all the studied reactive species are involved in the degradation process of DS and the contribution order is $h^+ > O_2^- > OH$ (see Figure 8c). The photodegradation efficiency of DS under different scavengers in the photocatalytic systems of Ag_3PO_4, as described in Figure 8d, indicates the important influence of OH and h^+ on DS photodegradation. However, in the $CuBi_2O_4/Ag_3PO_4$ (1:1) composite photocatalytic system (see Figure 8e), O_2^- and OH are the main reactive species for DS degradation and the influence of h^+ is weak. Thus, there is a difference of the reactive species involved in the same pollutant degradation process under the different photocatalysis systems, finally leading to the differentiated photocatalytic mechanism of the catalysts.
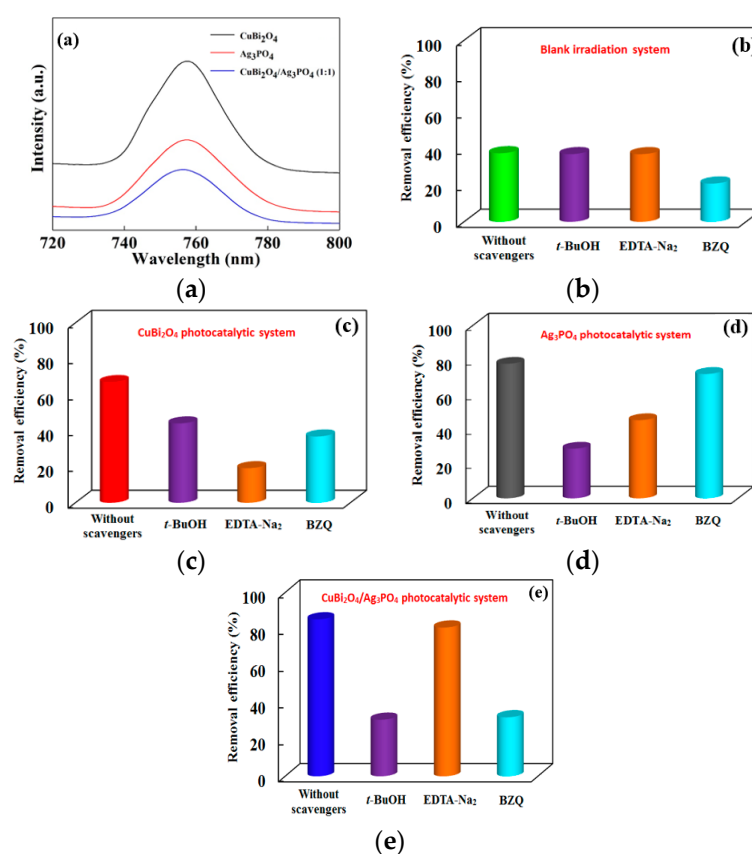

Figure 8. (**a**) Room temperature photoluminescence (PL) spectra of the as-prepared catalysts and photodegradation efficiency of DS under different scavengers in the photocatalytic systems of (**b**) blank irradiation, (**c**) $CuBi_2O_4$, (**d**) Ag_3PO_4, and (**e**) $CuBi_2O_4/Ag_3PO_4$ (1:1).

On the basis of the results described above, the photolysis mechanisms of the blank irradiation, $CuBi_2O_4$, Ag_3PO_4, and $CuBi_2O_4/Ag_3PO_4$ reaction systems were proposed. In the blank irradiation system, DS should first absorb actinic photons and change to be DS *, then two processes may occur: (1) the direct photodegradation process of DS * and (2) the photooxidation process of DS; that is, the DS * reacts with the dissolved O_2 to form O_2^-, which is subsequently involved in the degradation of DS. Because of the free radical capture experiment suggesting the O_2^- has a significant effect on the DS degradation in the blank irradiation system, the photooxidation process of DS is the dominated process. This speculation has also been put forward in a previous paper [49], and the transition of photogenerated electrons and holes is described in Figure 9a. In the $CuBi_2O_4$ photocatalytic system, the electron–hole ($e^- – h^+$) pairs will generate under the visible light irradiation and, then, the e^- and h^+ will induce to form other active radicals (such as O_2^- and OH) during the separation/migration processes. Due to the oxidation potential of OH^-/OH (1.99 eV) [27] being much higher than the potential of the

valence band of $CuBi_2O_4$ (E_{VB} = 0.95 eV), the OH cannot be induced by the h^+. However, the O_2 absorbed on the surface of the catalyst can be induced to be O_2^-, owing to the lower position of the standard redox potential of O_2/O_2^- (0.13 eV) [50] than the potential of the conduction band (E_{CB} = −0.77 eV). Then, the partial $O_2^{\bullet-}$ can be further induced to be OH (see Figure 9b). Therefore, the separated h^+ and the induced $O_2^{\bullet-}/OH^{\bullet}$ are involved in the degradation of DS. As for the photocatalytic system of Ag_3PO_4, the transition of photogenerated e^- and h^+ are described in Figure 9c and the photogenerated h^+ can be induced to form the active radical of $OH^{\bullet}$, whereas the photogenerated e^- could not be induced to form $O_2^{\bullet-}$ because of the higher position of the standard redox potential of O_2/O_2^- than the potential of the conduction band (E_{CB} = 0.25 eV). Then, the separated e^- should be easily captured by the Ag^+ coming from the lattice of the Ag_3PO_4, leading to the Ag^0 deposition on the surface of catalyst. This phenomenon seriously influences the photocatalytic activity and stability of Ag_3PO_4. When the semiconductor of Ag_3PO_4 is combined with $CuBi_2O_4$ to form the composite photocatalyst of $CuBi_2O_4/Ag_3PO_4$, the formed Ag^0 during the photocatalytic reaction process deposits on the surface of the catalyst and serves as the recombination center for the photogenerated e^- from CB of Ag_3PO_4 and the h^+ from VB of $CuBi_2O_4$, resulting in the aggregation of the photogenerated h^+ in the VB of Ag_3PO_4 and in the aggregation of the photogenerated e^- in the CB of $CuBi_2O_4$. Thus, the formation of O_2^- induced by e^- from the CB of $CuBi_2O_4$ and the formation of OH induced by h^+ from the VB of Ag_3PO_4 will be strong. From the free radical capture experiments, the effect of h^+ on the photodegradation of DS is extremely weak, suggesting that h^+ is mainly involved in the formation of OH. The detailed transition of photogenerated e^- and h^+ in a photocatalytic system of $CuBi_2O_4/Ag_3PO_4$ is represented in Figure 9d, and its photocatalytic mechanism is consistent with the Z-Scheme theory [28].
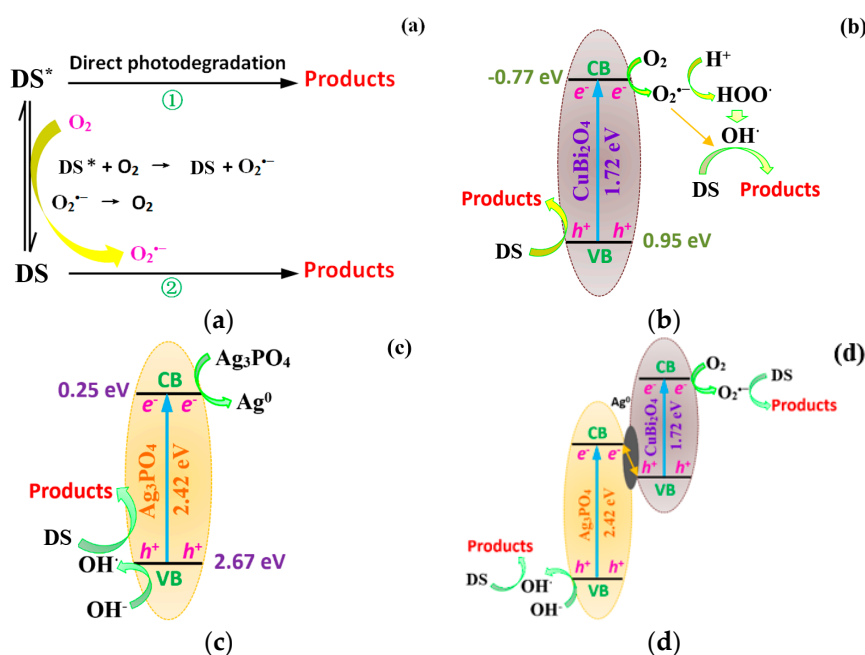

Figure 9. Transition of photogenerated electrons and holes in different photocatalytic system of (**a**) blank irradiation, (**b**) $CuBi_2O_4$, (**c**) Ag_3PO_4, and (**d**) $CuBi_2O_4/Ag_3PO_4$.

4. Conclusions

Ag_3PO_4 was deposited on $CuBi_2O_4$ to construct Z-scheme photocatalyst, and it was used for DS degradation. $CuBi_2O_4/Ag_3PO_4$ exhibited an excellent photocatalytic performance under the system of visible-light irradiation. Free radical capture experiments suggest the active species of O_2^- and OH contribute to the degradation of DS. Moreover, Z-Scheme theory can be used to explain the catalytic mechanism of $CuBi_2O_4/Ag_3PO_4$, and the formed Ag^0 during the reaction process serves as

the recombination center for the photogenerated e^- from CB of Ag_3PO_4 and the h^+ from VB of $CuBi_2O_4$, which improved the separation of photogenerated carriers, finally leading to the enhancement of the catalytic performance.

References

1. Sun, K.; Shi, Y.; Wang, X.; Li, Z. Sorption and retention of diclofenac on zeolite in the presence of cationic surfactant. *J. Hazard. Mater.* **2016**, *323*, 584–592. [CrossRef] [PubMed]

2. Cheikh, D.; García-Villén, F.; Majdoub, H.; Zayani, M.B.; Viseras, C. Complex of chitosan pectin and clay as diclofenac carrier. *Appl. Clay Sci.* **2019**, *172*, 155–164. [CrossRef]

3. Goldstein, M.; Shenker, M.; Chefetz, B. Insights into the Uptake Processes of Wastewater-Borne Pharmaceuticals by Vegetables. *Environ. Sci. Technol.* **2014**, *48*, 5593–5600. [CrossRef] [PubMed]

4. Espino-Estévez, M.R.; Fernández-Rodríguez, C.; González-Díaz, O.M.; Araña, J.; Espinós, J.P.; Ortega-Méndez, J.A.; Doña-Rodríguez, J.M. Effect of TiO_2-Pd and TiO_2-Ag on the photocatalytic oxidation of diclofenac, isoproturon and phenol. *Chem. Eng. J.* **2016**, *298*, 82–95. [CrossRef]

5. Bouju, H.; Nastold, P.; Beck, B.; Hollender, J.; Corvini, P.F.X.; Wintgens, T. Elucidation of biotransformation of diclofenac and 4'hydroxydiclofenac during biological wastewater treatment. *J. Hazard. Mater.* **2016**, *301*, 443–452. [CrossRef] [PubMed]

6. Wang, Y.; Liu, H.; Xie, Y.; Ni, T.; Liu, G. Oxidative removal of diclofenac by chlorine dioxide: Reaction kinetics and mechanism. *Chem. Eng. J.* **2015**, *279*, 409–415. [CrossRef]

7. Kohay, H.; Izbitski, A.; Mishael, Y.G. Developing polycation-clay sorbents for efficient filtration of diclofenac: Effect of dissolved organic matter and comparison to activated carbon. *Environ. Sci. Technol.* **2015**, *49*, 9280–9288. [CrossRef]

8. Bhadra, B.N.; Seo, P.W.; Jhung, S.H. Adsorption of diclofenac sodium from water using oxidized activated carbon. *Chem. Eng. J.* **2016**, *301*, 27–34. [CrossRef]

9. Miranda-García, N.; Suárez, S.; Sánchez, B.; Coronado, J.M.; Malato, S.; Maldonado, M.I. Photocatalytic degradation of emerging contaminants in municipal wastewater treatment plant effluents using immobilized TiO_2 in a solar pilot plant. *Appl. Catal. B Environ.* **2011**, *103*, 294–301. [CrossRef]

10. Bae, S.; Kim, D.; Lee, W. Degradation of diclofenac by pyrite catalyzed Fenton oxidation. *Appl. Catal. B Environ.* **2013**, *134*, 93–102. [CrossRef]

11. Chen, W.; Li, X.; Pan, Z.; Ma, S.; Li, L. Effective mineralization of Diclofenac by catalytic ozonation using Fe-MCM-41 catalyst. *Chem. Eng. J.* **2016**, *304*, 594–601. [CrossRef]

12. Tong, H.; Ouyang, S.; Bi, Y.; Umezawa, N.; Oshikiri, M.; Ye, J. Nano-photocatalytic materials: Possibilities and challenges. *Adv. Mater.* **2012**, *24*, 229–251. [CrossRef] [PubMed]

13. Chen, C.; Ma, W.; Zhao, J. ChemInform Abstract: Semiconductor-mediated photodegradation of pollutants under visible-light irradiation. *Chem. Soc. Rev.* **2010**, *39*, 4206–4219. [CrossRef] [PubMed]

14. Buama, S.; Junsukhon, A.; Ngaotrakanwiwat, P.; Rangsunvigit, P. Validation of energy storage of TiO_2NiO/TiO_2 film by electrochemical process and photocatalytic activity. *Chem. Eng. J.* **2017**, *309*, 866–872. [CrossRef]

15. Umer, M.; Tahir, M.; Azam, M.U.; Tahir, B.; Jaffar, M.M.; Alias, H. Montmorillonite dispersed single wall carbon nanotubes (SWCNTs)/TiO_2 heterojunction composite for enhanced dynamic photocatalytic H_2 production under visible light. *Appl. Clay Sci.* **2019**, *174*, 110–119. [CrossRef]

16. Yang, Z.M.; Huang, G.F.; Huang, W.Q.; Wei, J.M.; Yan, X.G.; Liu, Y.Y.; Jiao, C.; Wan, Z.; Pan, A. Novel Ag_3PO_4/CeO_2 composite with high efficiency and stability for photocatalytic applications. *J. Mater. Chem. A* **2014**, *2*, 1750–1756. [CrossRef]

17. Wang, W.; Zhu, Q.; Dai, Q.; Wang, X. Fe doped CeO_2 nanosheets for catalytic oxidation of 1, 2-dichloroethane: Effect of preparation method. *Chem. Eng. J.* **2016**, *307*, 1037–1046. [CrossRef]

18. Liu, M.; Hou, L.A.; Xi, B.D.; Li, Q.; Hu, X.; Yu, S. Magnetically separable Ag/AgCl-zero valent iron particles modified zeolite X heterogeneous photocatalysts for tetracycline degradation under visible light. *Chem. Eng. J.* **2016**, *302*, 475–484. [CrossRef]

19. Ye, Z.; Li, J.; Zhou, M.; Wang, H.; Ma, Y.; Huo, P.; Yu, L.; Yan, Y. Well-dispersed nebula-like ZnO/CeO_2@HNTs heterostructure for efficient photocatalytic degradation of tetracycline. *Chem. Eng. J.* **2016**, *304*, 917–933. [CrossRef]

20. Papoulis, D. Halloysite based nanocomposites and photocatalysis: A Review. *Appl. Clay Sci.* **2019**, *168*, 164–174. [CrossRef]

21. Yi, Z.; Ye, J.; Kikugawa, N.; Kako, T.; Ouyang, S.; Stuart-Williams, H.; Yang, H.; Cao, J.; Luo, W.; Li, Z. An orthophosphate semiconductor with photooxidation properties under visible-light irradiation. *Nat. Mater.* **2010**, *9*, 559–564. [CrossRef] [PubMed]

22. Jiao, Z.; Zhang, Y.; Yu, H.; Lu, G.; Ye, J.; Bi, Y. Concave trisoctahedral Ag_3PO_4 microcrystals with high-index facets and enhanced photocatalytic properties. *Chem. Commun.* **2013**, *49*, 636–638. [CrossRef] [PubMed]

23. Yu, H.; Jiao, Z.; Jin, B.; Feng, C.; Lu, G.; Bi, Y. Facile synthesis of porous Ag_3PO_4 photocatalysts with high self-stability and activity. *RSC Adv.* **2016**, *6*, 56166–56169. [CrossRef]

24. Zhang, S.; Zhang, S.; Song, L. Super-high activity of Bi^{3+} doped Ag_3PO_4 and enhanced photocatalytic mechanism. *Appl. Catal. B Environ.* **2014**, *152–153*, 129–139. [CrossRef]

25. Zhang, S.; Zhang, S.; Song, L. Co(II)-grafted Ag_3PO_4 photocatalysts with unexpected photocatalytic ability: Enhanced photogenerated charge separation efficiency, photocatalytic mechanism and activity. *J. Hazard. Mater.* **2015**, *293*, 72–80. [CrossRef] [PubMed]

26. Eswar, K.R.; Katkar, V.V.; Ramamurthy, P.C.; Madras, G. Novel $AgBr/Ag_3PO_4$ Decorated Ceria Nanoflake Composites for Enhanced Photocatalytic Activity toward Dyes and Bacteria under Visible Light. *Ind. Eng. Chem. Res.* **2015**, *54*, 8031–8042. [CrossRef]

27. Guo, J.; Ouyang, S.; Zhou, H.; Kako, T.; Ye, J. $Ag_3PO_4/In(OH)_3$ Composite Photocatalysts with Adjustable Surface-Electric Property for Efficient Photodegradation of Organic Dyes under Simulated Solar-Light Irradiation. *J. Phys. Chem. C* **2013**, *117*, 17716–17724. [CrossRef]

28. Zhou, P.; Yu, J.; Jaroniec, M. All-Solid-State Z-Scheme Photocatalytic Systems. *Adv. Mater.* **2014**, *26*, 4920–4935. [CrossRef] [PubMed]

29. Song, L.; Yang, J.; Zhang, S. Enhanced photocatalytic activity of Ag_3PO_4 photocatalyst via glucose-based carbonsphere modification. *Chem. Eng. J.* **2017**, *309*, 222–229. [CrossRef]

30. Liu, X.Q.; Chen, W.J.; Jiang, H. Facile synthesis of $Ag/Ag_3PO_4/AMB$ composite with improved photocatalytic performance. *Chem. Eng. J.* **2017**, *308*, 889–896. [CrossRef]

31. Peng, H.; Zhang, D.; Liu, X.; Tang, W.; Wan, H.; Xiong, H.; Ma, R. Facile synthesis and characterization of core-shell structured Ag_3PO_4@Hal nanocomposites for enhanced photocatalytic properties. *Appl. Clay Sci.* **2017**, *141*, 132–137. [CrossRef]

32. Cao, D.; Nasori, N.; Wang, Z.; Mi, Y.; Wen, L.; Yang, Y.; Qu, S.; Wang, Z.; Lei, Y. p-Type $CuBi_2O_4$: An easily accessible photocathodic material for high-efficiency water splitting. *J. Mater. Chem. A* **2016**, *4*, 8995–9001. [CrossRef]

33. Oh, W.D.; Lua, S.K.; Dong, Z.; Lim, T.T. Rational design of hierarchically-structured $CuBi_2O_4$ composites by deliberate manipulation of the nucleation and growth kinetics of $CuBi_2O_4$ for environmental applications. *Nanoscale* **2016**, *8*, 2046–2054. [CrossRef] [PubMed]

34. Chen, X.J.; Dai, Y.Z.; Guo, J.; Liu, T.H.; Wang, X.Y. Novel Magnetically Separable Reduced Graphene Oxide (RGO)/$ZnFe_2O_4$/Ag_3PO_4 Nanocomposites for Enhanced Photocatalytic Performance toward 2,4-Dichlorophenol under Visible Light. *Ind. Eng. Chem. Res.* **2015**, *55*, 568–578. [CrossRef]

35. Wang, M. N-type hedgehog-like $CuBi_2O_4$ hierarchical microspheres: Room temperature synthesis and their photoelectrochemical properties. *CrystEngComm* **2015**, *17*, 4019–4025. [CrossRef]

36. Oh, W.D.; Lua, S.K.; Dong, Z.; Lim, T.T. A novel three-dimensional spherical $CuBi_2O_4$ nanocolumn arrays with persulfate and peroxymonosulfate activation functionalities for 1H-benzotriazole removal. *Nanoscale* **2015**, *7*, 8149–8158. [CrossRef] [PubMed]

37. Patil, R.; Kelkar, S.; Naphade, R.; Ogale, S. Low temperature grown $CuBi_2O_4$ with flower morphology and its composite with CuO nanosheets for photoelectrochemical water splitting. *J. Mater. Chem. A* **2014**, *2*, 3661–3668. [CrossRef]

38. Xie, Y.; Zhang, Y.; Yang, G.; Liu, C.; Wang, J. Hydrothermal synthesis of $CuBi_2O_4$ nanosheets and their photocatalytic behavior under visible light irradiation. *Mater. Lett.* **2013**, *107*, 291–294. [CrossRef]

39. Zhang, L.; Zhang, H.; Huang, H.; Liu, Y.; Kang, Z. Ag_3PO_4/SnO_2 semiconductor nanocomposites with enhanced photocatalytic activity and stability. *New J. Chem.* **2012**, *36*, 1541–1544. [CrossRef]

40. Zhang, Y.; Xie, Y.; Li, J.; Bai, T.; Wang, J. Photocatalytic activity and adsorption performance of p-$CuBi_2O_4$/n-TiO_2 p-n heterojunction composites prepared by in situ sol-gel coating method. *J. Sol-Gel Sci. Technol.* **2014**, *71*, 38–42. [CrossRef]

41. Yuvaraj, S.; Karthikeyan, K.; Kalpana, D.; Lee, Y.S.; Selvan, R.K. Surfactant-free hydrothermal synthesis of hierarchically structured spherical $CuBi_2O_4$ as negative electrodes for Li-ion hybrid capacitors. *J. Colloid Interface Sci.* **2016**, *469*, 47–56. [CrossRef] [PubMed]

42. Vu, T.A.; Dao, C.D.; Hoang, T.T.T.; Dang, P.T.; Tran, H.T.K.; Nguyen, K.T.; Le, G.H.; Nguyen, T.V.; Lee, G.D. Synthesis of novel silver vanadates with high photocatalytic and antibacterial activities. *Mater. Lett.* **2014**, *123*, 176–180. [CrossRef]

43. Teng, W.; Li, X.; Zhao, Q.; Chen, G. Fabrication of $Ag/Ag_3PO_4/TiO_2$ heterostructure photoelectrodes for efficient decomposition of 2-chlorophenol under visible light irradiation. *J. Mater. Chem. A* **2013**, *1*, 9060–9068. [CrossRef]

44. Xu, Y.S.; Zhang, W.D. Morphology-controlled synthesis of Ag_3PO_4 microcrystals for high performance photocatalysis. *CrystEngComm* **2013**, *27*, 5407–5411. [CrossRef]

45. Elaziouti, A.; Laouedj, N.; Bekka, A. Synergetic effects of Sr-doped $CuBi_2O_4$ catalyst with enhanced photoactivity under UVA-light irradiation. *Environ. Sci. Pollut. Res.* **2015**, *23*, 15862–15876. [CrossRef] [PubMed]

46. Xu, J.W.; Gao, Z.D.; Han, K.; Liu, Y.; Song, Y.Y. Synthesis of Magnetically Separable $Ag_3PO_4/TiO_2/Fe_3O_4$ Heterostructure with Enhanced Photocatalytic Performance under Visible Light for Photoinactivation of Bacteria. *ACS Appl. Mater. Interfaces* **2014**, *6*, 15122–15131. [CrossRef] [PubMed]

47. Ming, G.; Na, Z.; Zhao, Y.; Jing, L.; Lu, L. Sunlight-Assisted Degradation of Dye Pollutants in Ag_3PO_4 Suspension. *Ind. Eng. Chem. Res.* **2012**, *51*, 5167–5173.

48. Patil, R. Low temperature grown $CuBi_2O_4$ with flower morphology and its composite with CuO nanosheets for photoelectrochemical water splitting. *Bioorg. Med. Chem. Lett.* **2014**, *19*, 92–95. [CrossRef]

49. Zhang, N.; Liu, G.; Liu, H.; Wang, Y.; He, Z.; Wang, G. Diclofenac photodegradation under simulated sunlight: Effect of different forms of nitrogen and kinetics. *J. Hazard. Mater.* **2011**, *192*, 411–418. [CrossRef]

50. Liu, W.; Wang, M.; Xu, C.; Chen, S.; Fu, X. Ag_3PO_4/ZnO: An efficient visible-light-sensitized composite with its application in photocatalytic degradation of Rhodamine B. *Mater. Res. Bull.* **2013**, *48*, 106–113. [CrossRef]